Linear Structural Dynamics and Tip-Vane Attitude Control for Square Solar Sails

Soroosh Hassanpour* and Christopher J. Damaren†

University of Toronto, Toronto, Ontario M3H 5T6, Canada

This Paper presents a linear model for a square solar sail spacecraft containing four pretensioned triangular sails supported by four flexible diagonal booms. The structural dynamics of the stretched sails and diagonal booms is explored by using a two-stage model including a static finite element or analytic model to solve for the sails in-plane stresses due to prestretching and a dynamic finite element model to calculate the in- and out-of-plane deflections of the interconnected sails and booms. The dynamic finite element model takes into account the effect of in-plane stresses, which are calculated by the static finite element or analytic model. Once the structural dynamic model is established, different modal cost analyses are used to evaluate and rank elastic modes of the solar sail. Two attitude controllers are developed for the solar sail, and the controller/structure interactions are studied using the linear model and considering an attitude maneuver.

Nomenclature

A	=	area
$\mathcal{B}$	=	control input (matrix)
C	=	boundary curve
$\mathcal{C}$	=	measurement output (matrix)
E	=	Young's modulus
$\boldsymbol{F}$	=	torque to force conversion (matrix)
$\mathcal{F}$	=	frame
$\boldsymbol{f}$	=	force
h	=	sail thickness
I	=	second moment of cross-sectional area
$\mathcal{K}$	=	stiffness (matrix)
k	=	controller coefficient
L	=	length
$\mathcal{M}$	=	mass (matrix)
m	=	general mass
$\boldsymbol{n}$	=	normal unit vector
$\boldsymbol{p}$	=	position with respect to inertial frame
P	=	point
$\mathcal{Q}$	=	generalized force
$\boldsymbol{q}$	=	generalized coordinate
$\boldsymbol{R}$	=	translational-to-rotational-coordinates conversion (matrix)
$\boldsymbol{r}$	=	rigid position of mass element with respect to body frame
S	=	surface
$\boldsymbol{s}$	=	sun unit vector
$\boldsymbol{T}$	=	torque
$\mathcal{T}$	=	kinetic energy
t	=	time
$\boldsymbol{U}$	=	body frame displacement (position) with respect to inertial frame
$\mathcal{U}$	=	potential energy
$\boldsymbol{u}$	=	elastic displacement with respect to body frame
$\mathcal{W}$	=	work
w	=	weighting coefficient
x	=	spatial coordinate
$\boldsymbol{y}$	=	sensor measurements vector
$\boldsymbol{z}$	=	actuator actions vector
$\boldsymbol{\Theta}$	=	body frame rotational displacement with respect to inertial frame
$\boldsymbol{\Omega}$	=	body frame rotational velocity with respect to inertial frame
α	=	vane rotation (angular degree of freedom)
δ	=	virtual (displacement or work)
$\boldsymbol{\varepsilon}$	=	vector part of quaternion
η	=	scalar part of quaternion
θ	=	body frame Euler angle with respect to inertial frame
ν	=	Poisson's ratio
ρ	=	density
σ	=	stress
τ	=	boundary traction
ω	=	natural frequency
$\mathbb{1}$	=	identity (matrix)
$\|\square\|$	=	Euclidean norm (2-norm) operator

Subscripts

B	=	body
b	=	boom
c	=	control
d	=	desired
e	=	error
I	=	inertial
nor	=	normal
s	=	sail
shr	=	shear
ss	=	solar sail
v	=	vane (single vane)
vs	=	vanes (all four vanes)

Superscripts

C	=	curve or line (per unit length density)
P	=	point or concentrated
S	=	surface (per unit area density)
T	=	transpose operator
$\times$	=	skew-symmetric matrix associated with a vector cross product
$\circ$	=	time derivative with respect to body frame (rotating frame)

*Postdoctoral Fellow, Institute for Aerospace Studies, 4925 Dufferin Street. Member AIAA.

†Professor and Director, Institute for Aerospace Studies, 4925 Dufferin Street. Associate Fellow AIAA.

I. Introduction

SOLAR sailing is a method of propulsion that makes use of quantum packets of sunlight energy or more accurately the momentum carried by sunlight photons, known as solar radiation

pressure (SRP), to propel a spacecraft in space. The idea is based on the fact that forces due to SRP on a spacecraft are orders of magnitude larger and normally more steady and predictable than other space environmental forces such as those from solar wind, meteoroids, Newtonian drag, and magnetic field [1]; an ideal sail (i.e., a perfectly reflecting one) facing the sun at a distance of 1 astronomical unit will experience a pressure of 9.12 μN/m^2 (μPa) [2] (this is determined using the solar luminosity and the inverse square law for the ensuing energy flux). Solar sailing propulsion is known to reduce the overall mass of spacecraft and to be more efficient than conventional chemical propulsion for interplanetary (relatively close to the sun) and interstellar travels (requiring large velocity changes).

In recent years, large-scale, lightweight, deployable solar sails, so-called gossamer structures, have attracted lots of attention as a key enabling technology for use in new human and robotic exploration of the solar system. Design, analysis, and control of these structures are therefore becoming important challenges in meeting the goals of the future space technology road map. Since their introduction by Garwin in 1958 [3], solar sails have been the subject of much research in a wide range of disciplines. From a mechanical engineering point of view, research on solar sails can be categorized into orbits, trajectories, and missions; design, packaging, and deployment; structural dynamics; and trajectory (orbital), attitude, and shape control. Among these, studies on solar sail orbits and trajectories and on solar sail attitude control have attracted much more attention than studies of other aspects [2,4–6]. Reviews by McInnes [7], Macdonald [8], and Fu et al. [1] include a nice summary of many different studies on solar sail missions and trajectories. Fu et al. have also reviewed the numerous works on solar sail attitude control (most of them being based on rigid solar sail models).

There has been a number of studies that have explored the structural dynamics of solar sails. These studies are based on either the boom-dominant flexible models in which the sails are neglected and only the support booms are taken into account [9–11] or the geometrically nonlinear finite element models (FEMs) in which the potentially large in- and out-of-plane deformations of sails and booms are dynamically coupled together [6,12–18]. Many other researchers have used rigid solar sail models within their studies. This is despite the fact that considerations such as overall mass, characteristic acceleration, packaging, and deployment drive solar sail spacecraft to be large, very thin, and ultraflexible. To the best of our knowledge, there have been only a few preliminary studies on using structural models of solar sails for model order reduction and designing trajectory, attitude, and shape controllers (e.g., see [9,11,19–21]). Recall that the previously proposed solar sail attitude controllers, as summarized by Fu et al. [1], have been mainly designed (and even tested) based on rigid solar sail models.

The general lack of structural analysis of solar sails and use of that analysis in studying other aspects of solar sails is partially due to the proprietary nature of the designs. The aforementioned (over-simplified) boom-dominant models deliver no information about the dynamics of the sails that are the most important component of a solar sail. The aforementioned (high-fidelity) nonlinear finite element models suffer from convergence and validation problems and high computational costs [6,12,13,17,18]. Neither of these model classes may be extensively used for model-based analyses, such as design parameter optimization and controller development. There is, therefore, a need for a new structural model (class) to fill the large gap between the existing two model classes. While taking into account the effect of sail membranes, the new model should ideally remain linear. With a linear structural model, powerful modal analysis tools become available for model truncation (order reduction) and model-based optimal controller development [22–24].

This Paper is devoted to establishing a two-stage linear structural model for structural dynamics of solar sails that is easy to solve and allows for modal analysis. It is also illustrated how the developed linear model can be used for modal cost analysis, modal truncation, and attitude controllers development and examination.

II. Two-Stage Linear Structural Model

Common solar sail spacecraft are composed of some ultrathin membranes with a reflective coating, known as sails, supported by lightweight structures, usually called booms or spars, that are attached to a central hub [2,3,6,25]. Some designs have also suggested the use of four plates (vanes) attached to the tips of the supporting booms to help with the attitude control of the solar sail [2,4–6]. Such a solar sail spacecraft is shown in Fig. 1.

In a solar sail, the ultrathin sail membranes have almost no resistance against bending and are usually prestretched to keep their surface flat during spacecraft travel in space. In the presence of out-of-plane (lateral) loads, e.g., SRP, some billowing occurs within the sails such that the in-plane stresses could withstand the out-of-plane loads and transfer them to the support booms. The out-of-plane loads and deformations and also the in-plane deformations are known to change the in-plane stresses, which initially are a result of the sail pretensioning. It is a common practice in modeling solar sails to capture the couplings between the in-plane and out-of-plane loads and deformations by using a complex and computationally expensive geometrically nonlinear FEM [6,12,13,17,18]. However, there is some evidence to indicate that the nonlinear terms in these models do not significantly affect the dynamic behavior of solar sails. Indeed, the simulation results presented by Li et al. [19] and Zhang et al. [20] have demonstrated that (at least some of) the nonlinear terms have relatively small effects on the overall dynamics of a square solar sail spacecraft.

For a usual solar sail design, one can expect that out-of-plane loads, mainly due to the SRP and orbital/attitude/structural accelerations, are very small. Support booms in a solar sail are designed to withstand these small out-of-plane loads and accelerations without undergoing large out-of-plane deformations (as such large deformations defect solar sail performance and attitude controllability). Moreover, in-plane stresses are introduced in the sail membranes (by prestretching them) to ensure that sails do not experience any large billowing when subjected to out-of-plane loads and accelerations. The required in-plane stresses are relatively small considering the absence of gravity effects in space and the small magnitude of out-of-plane loads. It is also expected that a solar sail experiences in-plane loads and accelerations that are much (even orders of magnitude) smaller than out-of-plane ones. The in-plane deformations during the spacecraft operation would therefore be much (orders of magnitude) smaller than out-of-plane deformations.

For such a solar sail traveling in space, the changes in the in-plane stresses, including those changes due to out-of-plane billowing, will be insignificant. Consequently, the in-plane and out-of-plane structural dynamics of the solar sail may be decoupled, and one can derive the solar sail structural model as a combination of three linear submodels: a linear static structural submodel for in-plane deformations and stresses of prestretched sail membranes, a linear dynamic structural submodel for in-plane deformations of interconnected sails and booms, and a linear dynamic structural submodel for out-of-plane deformations of interconnected sails and booms. It is worthwhile to note that, as is the case with most of the previously presented geometrically nonlinear FEM models (except, e.g., the model developed by Choi and Damaren [17,18]), the wrinkling and slacking of the sail membranes and the variation of SRP due to shadowing or billowing (i.e., variation of the sail shape) are neglected in these submodels. One might argue that a linear
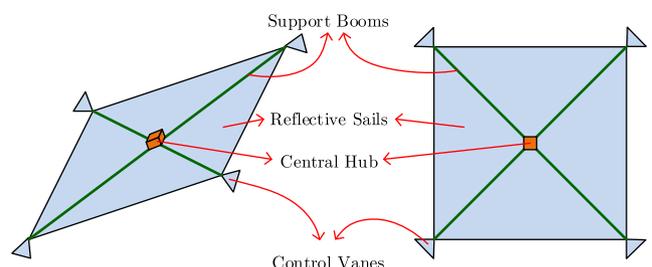

Fig. 1 Schematic configuration of a square solar sail.

structural dynamics model will not permit high-fidelity simulations in a large gossamer structure such as a solar sail, but it does allow us to address fundamental control issues such as the effects of sensor and actuator noncollocation.

A. Linear Static Structural Model of In-Plane Deformations and Stresses

Consider the traditional square solar sail, as shown in Fig. 1, with four triangular sails or quadrants that are stretched between four equal-length support booms. The quadrants can be connected together and to the booms at discrete points or continuously. This design is known to be robust enough for deployment in space and to be scalable to solar sails as large as 150 m on a side [26]. Because of the symmetry of the solar sail geometry, it is natural to assume that the pretensioning forces on the quadrants are similar and to solve for the in-plane stresses in only one of the quadrants.

An analytic model based on polynomial approximations/expansions has been proposed in [27] to calculate the in-plane stresses inside a quadrant that, as shown in Fig. 2, is under the action of some normal and shear traction distributions τ_{nor} and τ_{shr} on its boundaries 1 and 2. The boundary tractions, exerted by support booms on the sail during the deployment and preserved afterward, have been assumed to have a polynomial approximation form. To generalize the analytic model in [27], an FEM-based model for the prediction of static in-plane stresses and displacements will be developed and used in this work.

Consider the sail quadrant shown in Fig. 2, which is under static equilibrium conditions, and focus on the in-plane displacements. The potential energy $\mathcal{U}_s$ and virtual work $\delta\mathcal{W}_s$ expressions for the sail quadrant can be written as [28]

$$\mathcal{U}_s = \frac{1}{2}\left(\frac{E_s h_s}{1-\nu_s^2}\right)\iint_{A_s}\left(\left(\frac{\partial u_1}{\partial x_1}\right)^2 + \left(\frac{\partial u_2}{\partial x_2}\right)^2 + 2\nu_s\left(\frac{\partial u_1}{\partial x_1}\frac{\partial u_2}{\partial x_2}\right)\right.$$
$$\left. + \frac{1-\nu_s}{2}\left(\frac{\partial u_1}{\partial x_2} + \frac{\partial u_2}{\partial x_1}\right)^2\right)\mathrm{d}A_s \tag{1}$$

and

$$\delta\mathcal{W}_s = \iint_{A_s}(\delta u_1 f_1^S + \delta u_2 f_2^S)\,\mathrm{d}A_s + \oint_{C_s}(\delta u_1 f_1^C + \delta u_2 f_2^C)\,\mathrm{d}C_s$$
$$+ \sum_{P_s}(\delta u_1 f_1^P + \delta u_2 f_2^P) \tag{2}$$

where E_s, ν_s, and h_s are the quadrant Young's modulus, Poisson's ratio, and thickness; A_s and C_s are the quadrant area and boundary lines (curves); P_s are points of the quadrant where external point forces are applied; u_1 and u_2 are the in-plane elastic displacements in the x_1 and x_2 directions; and f_1^S, f_2^S and f_1^C, f_2^C and f_1^P, f_2^P are external surface, linear, and point forces applied to the sail quadrant. Now,
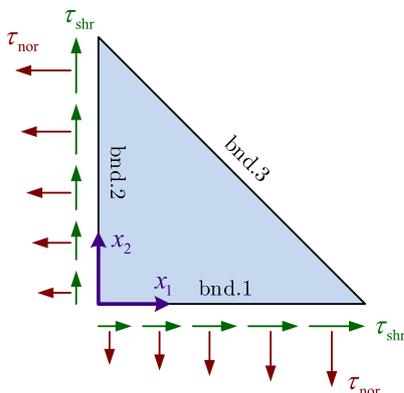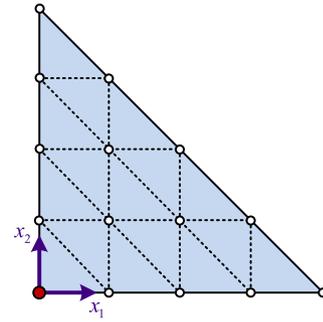

Fig. 3 A sail quadrant meshed with triangular membrane elements.

a linear FEM based on a three-node C^0-continuous triangular element with linear natural-coordinate basis functions [29,30] may be used to derive discretized linear static equations. The sail quadrant FEM model with a coarse (rough) mesh of triangular elements is shown in Fig. 3. The quadrant is assumed to be fixed (clamped) at the origin of $\mathcal{F}_B$.

By solving the discretized linear static equations, one will get the (nodal) displacement distributions, which can be used to calculate the in-plane stresses σ_{11}, σ_{22}, and σ_{12} as

$$\sigma_{11} = \frac{E_s}{1-\nu_s^2}\left(\frac{\partial u_1}{\partial x_1} + \nu_s\frac{\partial u_2}{\partial x_2}\right),$$
$$\sigma_{22} = \frac{E_s}{1-\nu_s^2}\left(\frac{\partial u_2}{\partial x_2} + \nu_s\frac{\partial u_1}{\partial x_1}\right),$$
$$\sigma_{12} = \frac{E_s}{1-\nu_s^2}\left(\frac{1-\nu_s}{2}\right)\left(\frac{\partial u_1}{\partial x_2} + \frac{\partial u_2}{\partial x_1}\right) \tag{3}$$

These static in-plane stresses will be fed into the dynamic structural model, which is explained in the following subsection.

B. Linear Dynamic Structural Model of In- and Out-of-Plane Deformations

Despite being decoupled (separated), the dynamic structural submodels for in- and out-of-plane deformations are explained simultaneously in this subsection. Consider again the square solar sail with four quadrants supported by four equal-length booms as shown in Fig. 4. The dynamics of such a solar sail is dependent on the dynamics of interconnected booms and sails. Assume that a body fixed frame $\mathcal{F}_B$ is attached to the solar sail center. This body frame $\mathcal{F}_B$ is used to represent the location and orientation of the solar sail with respect to an inertial reference frame $\mathcal{F}_I$.

Considering small elastic deformations (required to develop a linear model), the position of each mass element dm of the solar sail with respect to $\mathcal{F}_I$ can be expressed as

$$\boldsymbol{p} = \boldsymbol{U} + \boldsymbol{r} + \boldsymbol{u} \tag{4}$$

where $\boldsymbol{U}$ is the displacement (position) vector of $\mathcal{F}_B$ with respect to $\mathcal{F}_I$, $\boldsymbol{r}$ is the (rigid) position vector of dm with respect to $\mathcal{F}_B$, and $\boldsymbol{u}$ is

Fig. 2 One quadrant of a square solar sail under normal and shear boundary tractions (bnd., boundary).
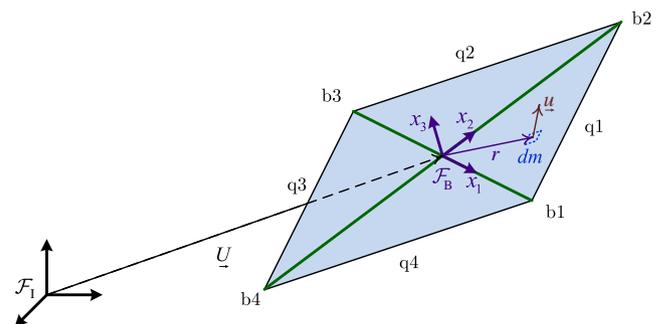

Fig. 4 Square solar sail with four booms and four quadrants along with inertial and body frames.

the vector of elastic displacements with respect to $\mathcal{F}_B$. The components of $\boldsymbol{u}$ in $\mathcal{F}_B$ are u_1, u_2, and u_3, representing the (dynamic or time-varying) in- and out-of-plane elastic displacements in the x_1, x_2, and x_3 directions, respectively. Note that the just-introduced (dynamic) in-plane displacements u_1 and u_2 are different from the (static) pretensioning in-plane displacements u_1 and u_2 introduced in Eq. (1) and should be added to (superimposed on) those to find the total in-plane displacements.

By differentiating Eq. (4) with respect to time, the velocity vector of each mass element is obtained as

$$\dot{\boldsymbol{p}} = \dot{\boldsymbol{U}} + \dot{\boldsymbol{r}} + \dot{\boldsymbol{u}} = \dot{\boldsymbol{U}} + \overset{\circ}{\boldsymbol{r}} + \boldsymbol{\Omega} \times \boldsymbol{r} + \overset{\circ}{\boldsymbol{u}} + \boldsymbol{\Omega} \times \boldsymbol{u} \approx \dot{\boldsymbol{U}} + \boldsymbol{\Omega} \times \boldsymbol{r} + \overset{\circ}{\boldsymbol{u}} \tag{5}$$

where $\overset{\circ}{\square}$ represents the time derivative with respect to $\mathcal{F}_B$ (which is a rotating frame), $\boldsymbol{\Omega}$ is the rotational velocity of $\mathcal{F}_B$ (which is assumed to be small so that $\boldsymbol{\Omega} \times \boldsymbol{u}$ is a second-order term and can be neglected), and note that rigid position vector $\boldsymbol{r}$ does not change in $\mathcal{F}_B$ (i.e., $\overset{\circ}{\boldsymbol{r}} = \boldsymbol{0}$). Similarly, the virtual displacement vector associated with each mass element can be written as [31]

$$\delta\boldsymbol{p} \approx \delta\boldsymbol{U} + \delta\boldsymbol{\Theta} \times \boldsymbol{r} + \delta\boldsymbol{u} \tag{6}$$

where $\delta\boldsymbol{\Theta}$ is the virtual rotational displacement vector of $\mathcal{F}_B$ with respect to $\mathcal{F}_I$. The relations of Eqs. (4–6) can be used within the approach explained by Choi and Damaren [17,18] to derive potential and kinetic energy and virtual work expressions of the solar sail.

To be more precise, the solar sail potential energy $\mathcal{U}_{ss}$ will be obtained as a summation of the potential energy of booms $\mathcal{U}_b$ and potential energy of sails $\mathcal{U}_s$,

$$\mathcal{U}_{ss} = \sum \mathcal{U}_b + \sum \mathcal{U}_s,$$
$$\mathcal{U}_b = \frac{1}{2} E_b A_b \int_{L_b} \left(\frac{\partial u_1}{\partial x_1}\right)^2 \mathrm{d}L_b + \frac{1}{2} E_b I_b \int_{L_b} \left(\frac{\partial^2 u_2}{\partial x_1^2}\right)^2 \mathrm{d}L_b$$
$$+ \frac{1}{2} E_b I_b \int_{L_b} \left(\frac{\partial^2 u_3}{\partial x_1^2}\right)^2 \mathrm{d}L_b,$$
$$\mathcal{U}_s = \frac{1}{2} \left(\frac{E_s h_s}{1 - \nu_s^2}\right) \iint_{A_s} \left(\left(\frac{\partial u_1}{\partial x_1}\right)^2 + \left(\frac{\partial u_2}{\partial x_2}\right)^2 + 2\nu_s \frac{\partial u_1}{\partial x_1}\frac{\partial u_2}{\partial x_2}\right)$$
$$+ \frac{1 - \nu_s}{2} \left(\frac{\partial u_1}{\partial x_2} + \frac{\partial u_2}{\partial x_1}\right)^2 \mathrm{d}A_s$$
$$+ \frac{1}{2} h_s \iint_{A_s} \left(\sigma_{11}\left(\frac{\partial u_3}{\partial x_1}\right)^2 + \sigma_{22}\left(\frac{\partial u_3}{\partial x_2}\right)^2 + 2\sigma_{12}\frac{\partial u_3}{\partial x_1}\frac{\partial u_3}{\partial x_2}\right) \mathrm{d}A_s \tag{7}$$

where E_b, A_b, and I_b are the boom Young's modulus, cross-sectional area, and second moment of the cross-sectional area; L_b is the boom length; and σ_{11}, σ_{22}, and σ_{12} are the static (constant) in-plane stresses precalculated by the static submodel in the previous subsection and given by Eq. (3). In Eq. (7), note that booms are assumed as long and slender linear Euler–Bernoulli beams (with small deformations) and sails are considered as ultrathin membranes with constant in-plane stresses and no bending resistance (or flexural rigidity/stiffness) [28]. The constant (static) in-plane stresses, established by prestretching the membranes, are assumed to be large compared to time-varying (dynamic) in-plane stresses due to lateral loads and deformations when the sail membranes are in action. The sail potential energy $\mathcal{U}_s$ in Eq. (7) contains the contribution from the in-plane deformations and the contribution from the coupling between the constant in-plane stresses and the lateral displacement u_3.

Analogously, the solar sail kinetic energy $\mathcal{T}_{ss}$ and virtual work $\delta\mathcal{W}_{ss}$ expressions will be

$$\mathcal{T}_{ss} = \sum \mathcal{T}_b + \sum \mathcal{T}_s,$$
$$\mathcal{T}_b = \frac{1}{2} \rho_b A_b \int_{L_b} (\dot{\boldsymbol{p}} \cdot \dot{\boldsymbol{p}}) \, \mathrm{d}L_b,$$
$$\mathcal{T}_s = \frac{1}{2} \rho_s h_s \iint_{A_s} (\dot{\boldsymbol{p}} \cdot \dot{\boldsymbol{p}}) \, \mathrm{d}A_s \tag{8}$$

and

$$\delta\mathcal{W}_{ss} = \sum \delta\mathcal{W}_b + \sum \delta\mathcal{W}_s,$$
$$\delta\mathcal{W}_b = \int_{L_b} (\delta\boldsymbol{p} \cdot \boldsymbol{f}^C) \, \mathrm{d}L_b + \sum_{P_b} (\delta\boldsymbol{p} \cdot \boldsymbol{f}^P),$$
$$\delta\mathcal{W}_s = \iint_{A_s} (\delta\boldsymbol{p} \cdot \boldsymbol{f}^S) \, \mathrm{d}A_s + \oint_{C_s} (\delta\boldsymbol{p} \cdot \boldsymbol{f}^C) \, \mathrm{d}C_s + \sum_{P_s} (\delta\boldsymbol{p} \cdot \boldsymbol{f}^P) \tag{9}$$

where $\dot{\boldsymbol{p}}$ is given by Eq. (5), ρ_b is the density of the boom, ρ_s is the density of the sail, $\delta\boldsymbol{p}$ is given by Eq. (6), and P_b are points of the boom where external point forces are applied.

Having the potential and kinetic energy and virtual work expressions, a linear FEM can be employed to derive discretized linear dynamic equations for the solar sail in the form

$$\mathcal{M}\ddot{\boldsymbol{q}} + \mathcal{K}\boldsymbol{q} = \mathcal{Q} \tag{10}$$

where $\boldsymbol{q}$ is the matrix of generalized coordinates and $\mathcal{M}$, $\mathcal{K}$, and $\mathcal{Q}$ are the finite element mass, stiffness, and generalized force matrices. Note that $\boldsymbol{q}$ contains the translational and (small) rotational displacements of $\mathcal{F}_B$ at the center of the solar sail represented in $\mathcal{F}_B$ (these are known as the rigid body translational and rotational displacements), i.e.,

$$\ddot{\boldsymbol{q}} = \begin{bmatrix} \ddot{\boldsymbol{U}} \\ \dot{\boldsymbol{\Omega}} \\ \ddot{\boldsymbol{u}} \end{bmatrix}, \qquad \dot{\boldsymbol{q}} = \begin{bmatrix} \dot{\boldsymbol{U}} \\ \boldsymbol{\Omega} \\ \dot{\boldsymbol{u}} \end{bmatrix}, \qquad \boldsymbol{q} = \begin{bmatrix} \boldsymbol{U} \\ \boldsymbol{\Theta} \\ \boldsymbol{u} \end{bmatrix} \tag{11}$$

where $\boldsymbol{u}$ is the column matrix of all elastic displacements at nodal points of the FEM. The linear dynamic equations are valid for solar sails undergoing small rigid body rotations and rotational velocities and accelerations (small $\boldsymbol{\Theta}$, $\boldsymbol{\Omega}$, and $\dot{\boldsymbol{\Omega}}$), small rigid body translational accelerations (small $\ddot{\boldsymbol{U}}$), and small elastic deformations (small $\boldsymbol{u}$). They can be used for modal analysis or can be integrated numerically for dynamic simulations.

In this work, the Hermitian beam elements (i.e., two-node C^1-continuous linear elements with cubic Hermite basis functions) are used to discretize the booms (i.e., Euler–Bernoulli beams), and three-node C^0-continuous triangular elements with linear natural-coordinate basis functions are employed to discretize the sails [29,30]. The schematic of the solar sail FEM model with a coarse (rough) mesh of linear and triangular elements is shown in Fig. 5.
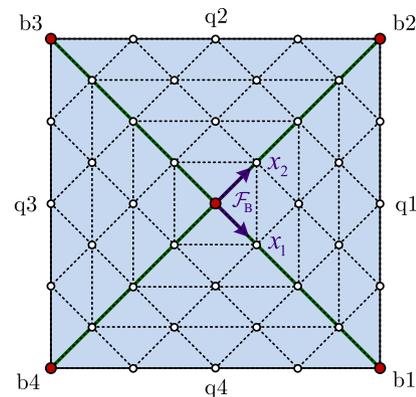

Fig. 5 A square solar sail meshed with triangular membrane and linear beam elements.

In the FEM model, booms are fixed (clamped) at the origin of $\mathcal{F}_B$, and sails are connected (pinned) to the booms at least at the origin of $\mathcal{F}_B$ and at the boom tips. If desired, it is possible to add more connection points between the sails and the booms at other nodal points along the diagonals. In addition, rigid masses can be added at the solar sail center and at the boom tips to represent the inertia of the central hub and payload and the inertia of the (relatively small) control tip vanes.

For solar sails with large rotational displacements (the rigid body translational acceleration $\ddot{U}$, the rigid body rotational velocities and accelerations Ω and $\dot{\Omega}$, and the elastic deformations u are still assumed to be small), the linear dynamic equations should be complemented with some kinematic equations. The kinematic equations enable integration of the rigid body translational accelerations represented in $\mathcal{F}_B$ (i.e., the $\ddot{U}$ part in $\ddot{q}$) and the rigid body rotational velocities described in $\mathcal{F}_B$ (i.e., Ω part in $\dot{q}$) to get the rigid body rotational and translational displacements. Using quaternions (Euler parameters) to parameterize the finite (large) rotations, these differential kinematic equations can be written as

$$^I\ddot{U} = \left(\mathbb{1} - 2\varepsilon^T\varepsilon\mathbb{1} + 2\varepsilon\varepsilon^T + 2\eta\varepsilon^\times\right)\ddot{U},$$

$$\begin{bmatrix} \dot{\varepsilon} \\ \dot{\eta} \end{bmatrix} = \frac{1}{2}\begin{bmatrix} -\Omega^\times & \Omega \\ -\Omega^T & 0 \end{bmatrix}\begin{bmatrix} \varepsilon \\ \eta \end{bmatrix} \qquad (12)$$

where $\square^T$ represents the transpose operator, $\square^\times$ denotes the skew-symmetric cross-product matrix associated with a vector $\mathbb{1}$, is the identity matrix, ε and η are the vector and scalar parts of the quaternion, $\ddot{U}$ and Ω are the descriptions of rigid body translational acceleration and rotational velocity vectors in $\mathcal{F}_B$, and $^I\ddot{U}$ is the description of translational acceleration vector in $\mathcal{F}_I$. Despite integrals of $\ddot{U}$ that do not have a physical meaning, successive integration of $^I\ddot{U}$ results in translational velocities and displacements in $\mathcal{F}_I$, i.e., $^I\dot{U}$ and ^IU. The differential kinematic equations in Eq. (12) will be solved alongside the dynamic equations in Eq. (10) to provide the rigid body motions of the solar sail.

Since visualization of encountered rotations from a given quaternion set is not obvious, the solar sail rigid body rotations (solar sail attitude) will be expressed in terms of x_1–x_2–x_3 Euler angles, denoted by θ_1, θ_2, and θ_3 representing sequential rotations of solar sail around x_1, x_2, and x_3 axes of the rotating body frame $\mathcal{F}_B$, when presenting the simulation results.

III.   Case Study

To illustrate the FEM-based linear structural dynamic model developed in the previous section and to undertake the desired modal cost analysis and modal truncation techniques, this section introduces a 150 m square solar sail available in the literature [6,19] that will be used in the rest of the Paper as a case study.

A.   Selected 150 m Square Solar Sail

Consider the 150 m five-point connected square solar sail design studied in [6]. The solar sail is composed of four booms and four triangular sail quadrants that are connected at five points, i.e., at the central hub and at the tip ends of booms. The booms are thin-walled tubes of radius 0.229 m and thickness 7.5 μm. The sail quadrants are right isosceles triangular membranes of thickness 2.5 μm. Each sail quadrant is pretensioned by applying concentrated forces at its three vertices. These forces are such that the von Mises stress at the triangular quadrant centroid is 6895 Pa (1 psi) and the sail quadrant is in static equilibrium (each force line of action passes through the triangular quadrant centroid). A 291.05 kg concentrated mass, representing the central bus, control mast, payload, and other equipment and instrumentation, is located at the center of solar sail. In this work, the moments of inertia associated with this concentrated mass are assumed to be 1014.35, 1014.35, and 36.56 kg · m^2, respectively, about the x_1, x_2, and x_3 axes of the body frame $\mathcal{F}_B$. A 0.58 kg concentrated mass representing a control tip vane is also located at the tip end of each boom. For the purpose of this work,

Table 1   Summary of the square solar sail model parameters

	Sails		Booms
L_s, m	$150/\sqrt{2}$	L_b, m	$150/\sqrt{2}$
A_s, m^2	5625	A_b, m^2	1.08×10^{-5}
h_s, m	2.50×10^{-6}	I_b, m^4	2.83×10^{-7}
ρ_s, kg/m^3	1572	ρ_b, kg/m^3	1908
E_s, Pa	2.48×10^9	E_b, Pa	124×10^9
ν_s	0.34	ν_b	0.30

the tip vanes are assumed to be double-sided reflective right isosceles triangles with a side length of 15 m, each having two angular degrees of freedom (DOF) with respect to its supporting boom. The other parameters needed by the linear structural model developed in the previous section are calculated and listed in Table 1 [6].

For such a solar sail, the FEM-based linear structural model developed in the previous section is used to derive discretized linear dynamic equations in a linear matrix-second-order form as given by Eqs. (10) and (12). Each boom is divided into 30 linear elements (31 nodes), and each sail is meshed with 900 triangular elements (496 nodes).

B.   Constrained and Unconstrained Mode Shapes

The natural frequencies and mode shapes of the 150 m solar sail are obtained using linear algebra. Figure 6 illustrates the first six mode shapes and their associated natural frequencies of the constrained solar sail in which $\mathcal{F}_B$ is fixed with respect to $\mathcal{F}_I$. In addition, the first six unconstrained nonrigid (elastic) mode shapes and their associated natural frequencies of the same solar sail are given in Fig. 7.

It is worthwhile to note that, employing geometrically nonlinear FEM, natural frequencies and mode shapes of the 150 m square solar sail have been derived and presented in multiple publications before [6,12,19,20]. It can be said that the natural frequencies obtained from the linear model are in the same range as those from the nonlinear models and there are satisfying similarities between the mode shapes of these models.
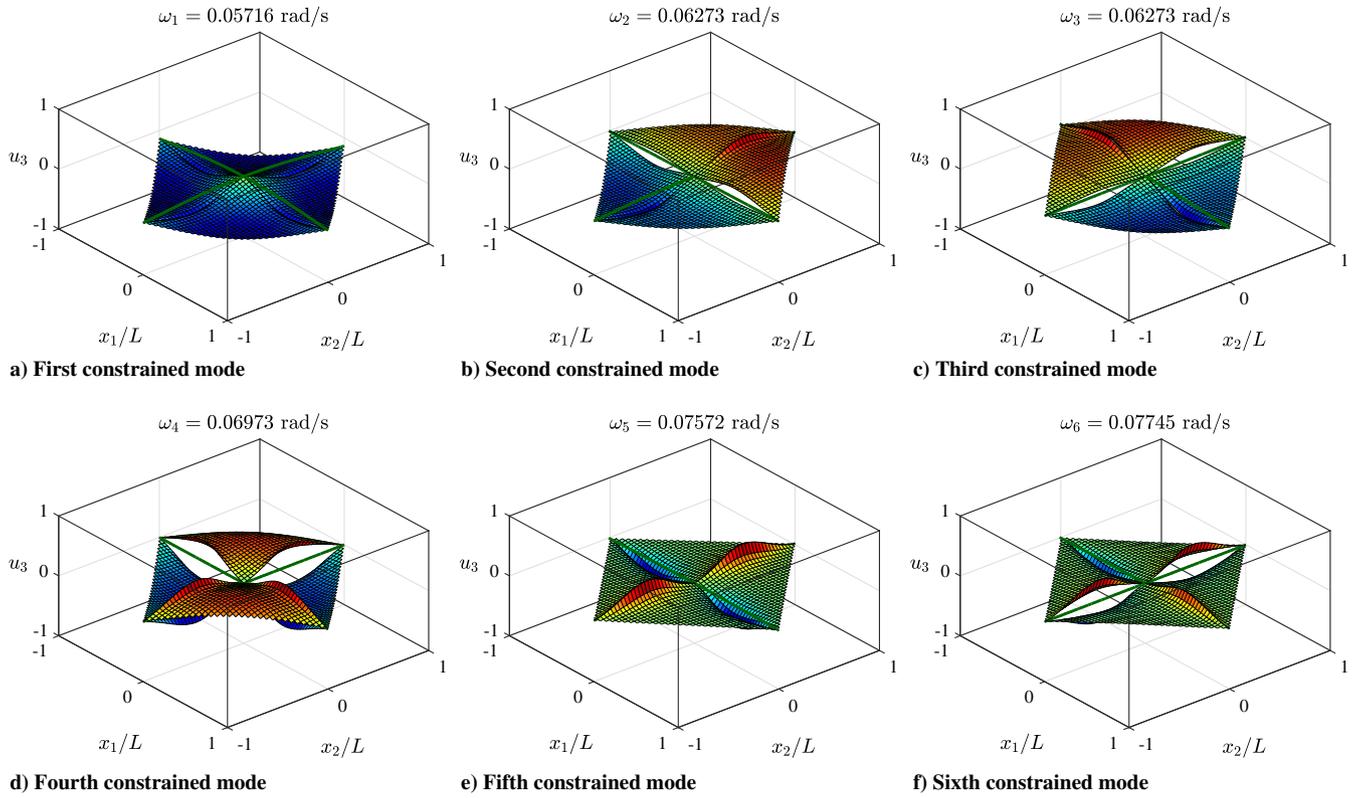
C.   Modal Cost Analysis

The FEM-based linear structural dynamic model developed in this work may be used within different studies to acquire important information about the dynamic behavior of solar sails. One such study is modal cost analysis, which requires a knowledge of mode shapes and natural frequencies of solar sail spacecraft.
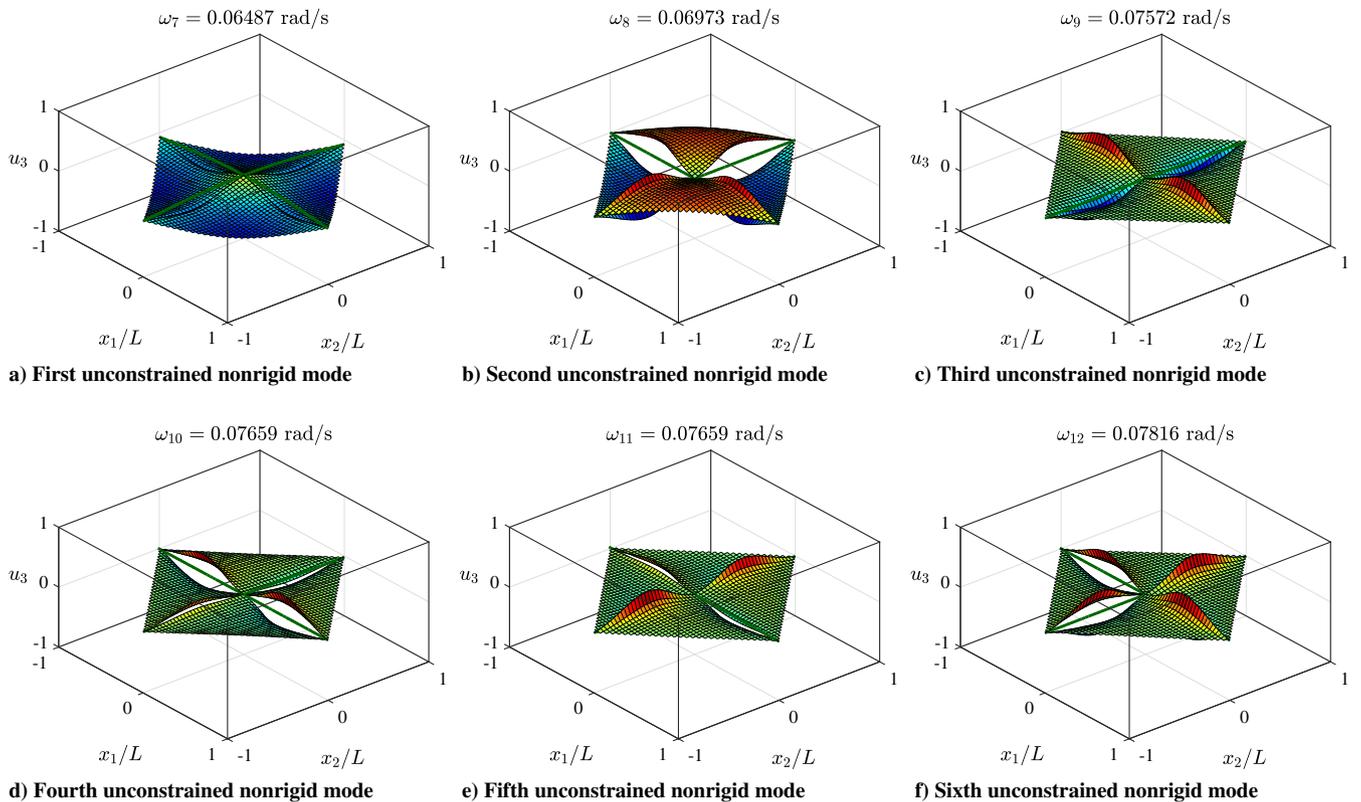
Modal cost analysis is of particular interest for studying solar sail spacecraft (and other so-called gossamer structures). These ultraflexible large space structures possess numerous low natural frequencies that are spaced very close to each other [32]. As a result, a natural-frequency-based truncation criteria may not be effective for model order reduction of these systems. Instead, mode-shape-based truncation techniques, such as those based on modal cost analysis, are required (usually in combination with the natural-frequency-based truncation criteria) to develop efficient control-oriented (reduced-order) models.

D.   Constrained Inertial Completeness Indices

A relatively simple criterion for evaluating modes of a flexible spacecraft is the modal inertial completeness index [23]. It measures the contribution of each mode of a flexible spacecraft to its effective translational and rotational inertia (or overall linear and angular momenta). The inertial completeness index can be calculated either based on the spacecraft constrained mode shapes or based on the spacecraft unconstrained nonrigid mode shapes. In this Paper, we consider the constrained inertial completeness index. It can be normalized with respect to the flexible inertia of the spacecraft [23]. For the 150 m square solar sail, the flexible inertia will be the inertia associated to the sails, booms, and control vanes, and the rigid inertia is the inertia corresponding to the central bus, control mast, payload, and other equipment and instrumentation located at the center of the solar sail.

$\omega_1 = 0.05716$ rad/s — a) First constrained mode

$\omega_2 = 0.06273$ rad/s — b) Second constrained mode

$\omega_3 = 0.06273$ rad/s — c) Third constrained mode

$\omega_4 = 0.06973$ rad/s — d) Fourth constrained mode

$\omega_5 = 0.07572$ rad/s — e) Fifth constrained mode

$\omega_6 = 0.07745$ rad/s — f) Sixth constrained mode

Fig. 6   The first six constrained mode shapes of the 150 m solar sail.

$\omega_7 = 0.06487$ rad/s — a) First unconstrained nonrigid mode

$\omega_8 = 0.06973$ rad/s — b) Second unconstrained nonrigid mode

$\omega_9 = 0.07572$ rad/s — c) Third unconstrained nonrigid mode

$\omega_{10} = 0.07659$ rad/s — d) Fourth unconstrained nonrigid mode

$\omega_{11} = 0.07659$ rad/s — e) Fifth unconstrained nonrigid mode

$\omega_{12} = 0.07816$ rad/s — f) Sixth unconstrained nonrigid mode

Fig. 7   The first six unconstrained nonrigid mode shapes of the 150 m solar sail.

The first and third plots in Fig. 8 illustrate the normalized constrained translational and rotational inertial completeness indices calculated for the first 50 modes of the considered square solar sail. For each mode in each of these plots, three indices are calculated, representing the contribution of that mode to the translation or rotation in the x_1, x_2, and x_3 directions. The natural frequencies are shown in the same plots for easy access (using downward bars). Note that indices corresponding to a mode are represented with bars that have small overlaps. The second and fourth plots of Fig. 8 show the cumulative value of constrained inertial completeness indices for the first 50 modes.
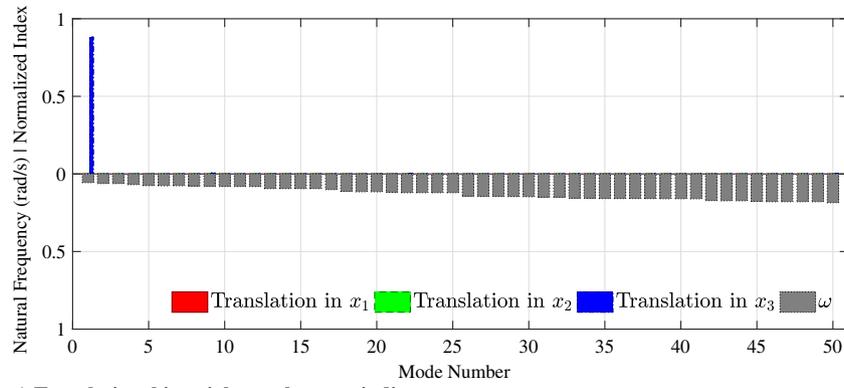
a) Translational inertial completeness indices
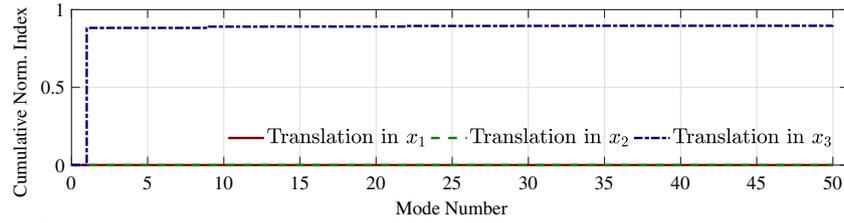
b) Cumulative translational inertial completeness indices
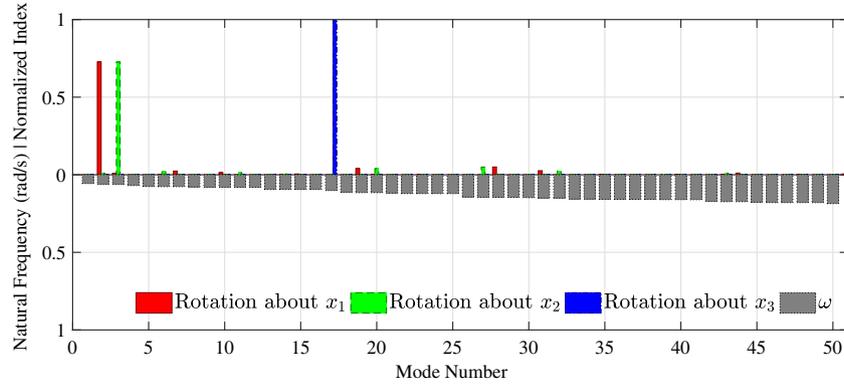
c) Rotational inertial completeness indices
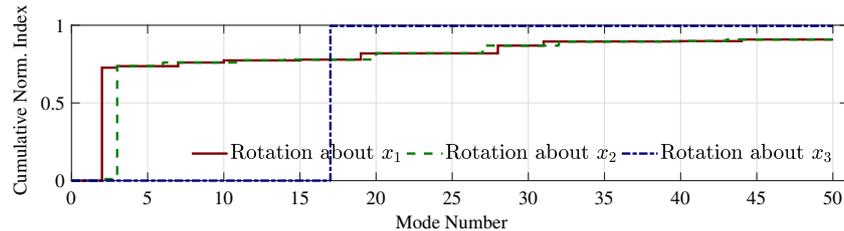
d) Cumulative rotational inertial completeness indices

Fig. 8   Normalized constrained inertial completeness indices of the 150 m solar sail (Norm., Normalized).

E. Controllability and Observability Indices

Other very useful criteria for weighting mode shapes of a flexible spacecraft are modal controllability and observability indices [23]. The controllability index illustrates the manner in which control actuation inputs (and potentially other external inputs) affect each mode. The observability index, on the other hand, indicates the way in which each mode is reflected by the sensor measurements. These criteria can be used to rank mode shapes of a flexible spacecraft as well as to optimize the position of actuators and sensors (measurements).

The main inputs to the selected solar sail are the distributed surface force from the SRP over the sail area, the (potential) point force and moment exerted by some actuators on the rigid mass at the center of the solar sail (central bus or hub), and the forces and moments from the control vanes at the tip of support booms. Considering the linear photonic thrust model for the SRP [33], the resulting distributed force would have not only a component normal to the sail plane but also

components within that plane. The point force and moment at the central bus may be provided by a micro- or nanothruster and a control moment gyro to form a hybrid attitude and trajectory control system along with the SRP and the control tip vanes. Finally, the force and moment from each tip vane may be simplified and assumed as only two lateral point force components perpendicular to the boom supporting that vane [17,18,34,35] (with this assumption, a nonlinear mapping between the angular DOF of each vane and its lateral force components is required). Assuming these forces and moments as (control) inputs to the solar sail spacecraft, one can rewrite the dynamic equations in Eq. (10) as

$$\mathcal{M}\ddot{q} + \mathcal{K}q = \mathcal{B}z \tag{13}$$

where $\mathcal{B}$ is the control input matrix and z is the column of actuator actions (control vector). Based on the aforementioned assumptions,

z contains 17 elements; three elements correspond to the components of the SRP in $\mathcal{F}_B$, 6 elements are associated with the components of the bus point force and moment in $\mathcal{F}_B$, and 8 elements represent the lateral point forces of four tip vanes in $\mathcal{F}_B$.

Using the unconstrained mode shapes of the selected 150 m square solar sail and the control input matrix $\mathcal{B}$, the normalized modal controllability indices are calculated and shown in the first two plots of Fig. 9. The controllability index associated with the SRP is shown in the first plot to determine which modes are most affected by this distributed force. The controllability indices associated with the central bus point force and moment and the tip-vane lateral forces as the key control inputs are of more interest and are represented separately in the second plot. Note that the controllability index corresponding to each input is normalized with respect to its own maximum value and therefore the first two plots of Fig. 9 should not be used to compare the controllability indices corresponding to different inputs.

For modal observability index calculation, some information about the location and type of sensor measurements (that are being used to determine the state of the spacecraft) is needed. Having this information, one may complement the dynamic equations in Eq. (13) and write

$$\mathcal{M}\ddot{q} + \mathcal{K}q = Bz,$$
$$y = \mathcal{C}q + \mathcal{C}'\dot{q} \tag{14}$$

where $\mathcal{C}$ and $\mathcal{C}'$ are measurement output matrices and y is the column of sensor measurements (output vector). In regard to the considered solar sail, it is of great advantage to assume the type and placement of the sensor measurements in such a way as to create a passive plant with collocated actuators and rate sensors, i.e., to form a dynamic system of the form Eq. (14) in which $\mathcal{C} = 0$ and $\mathcal{C}' = \mathcal{B}^T$. Such a collocated passive system is advantageous since it can be stabilized
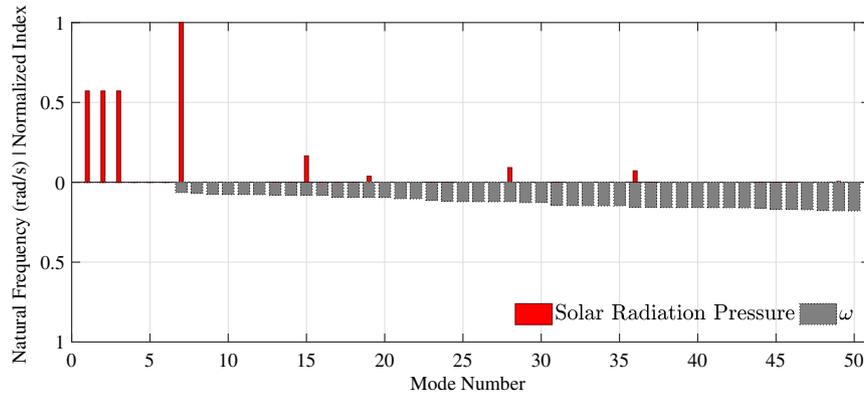
a) **Controllability index corresponding to solar radiation pressure as input**
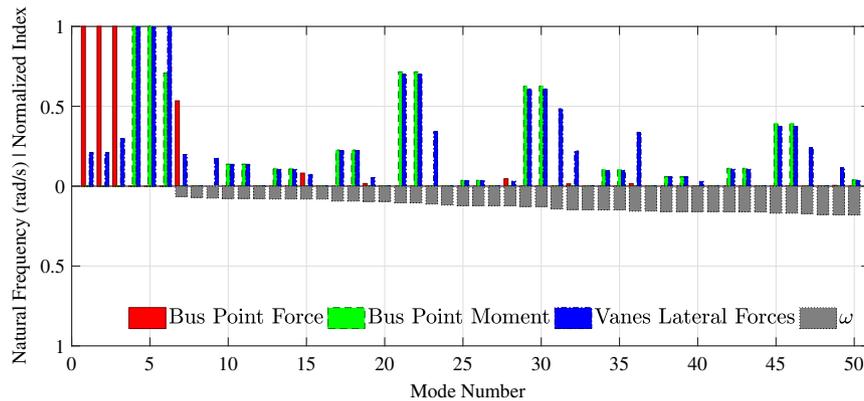
b) **Controllability indices corresponding to central bus point force and moment and vanes lateral forces as inputs**
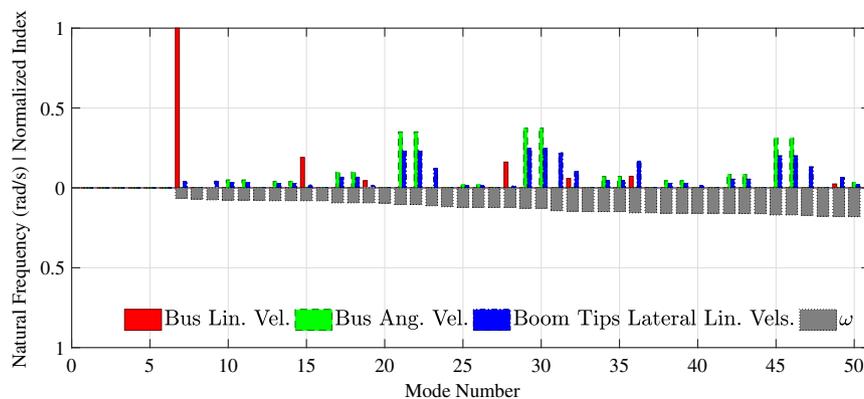
c) **Observability indices corresponding to central bus translational and rotational velocities and boom tips lateral translational velocities as outputs**

Fig. 9   **Normalized modal controllability and observability indices of the 150 m solar sail (Lin., linear; Vel., velocity; Ang., angular; Vels., velocities).**

Table 2 Summary of the retained 15 elastic modes in the truncated models (mode numbers sorted by their index values in descending order)

Truncation criterion	Modes type	Retained elastic modes
Completeness index	Constrained	17, 1, 2, 3, 27, 28, 19, 20, 66, 31, 32, 6, 7, 67, 68
Controllability index	Unconstrained	7, 61, 62, 21, 22, 29, 30, 137, 138, 98, 99, 105, 106, 71, 139

with a strictly positive real controller without worrying about the control and observation spillover [32,36].

Recalling the considered solar sail (with the central bus point force and moment and the vanes lateral point forces as the key control inputs), a collocated system may be achieved, provided rate sensors are used to measure the translational and rotational velocities at the solar sail central bus and the lateral (perpendicular) translational velocities at the boom tips (points where the control vanes are attached), all described in $\mathcal{F}_B$. Assuming such sensors and employing the unconstrained mode shapes and natural frequencies of the selected 150 m square solar sail, the modal observability indices are calculated and illustrated in the third plot of Fig. 9. Note that the observability indices in the third plot of Fig. 9 have trends similar to the controllability indices in the second plot. This is due to the fact that for a system with collocated actuators and rate sensors the modal observability index is equal to the modal controllability index multiplied by the mode natural frequency.

F. Modal Truncation

A direct application of the modal cost analysis is to derive reduced models by keeping only those modes with the highest contribution to the overall desired response (cost) of the spacecraft and truncating the modes with the smallest effects. It is worthwhile to note that the FEM-based discretized structural model with a finite (but usually very large) number of DOF can be considered as a reduced-order model of the infinite-dimensional distributed-parameter flexible solar sail. However, this model may still be quite large (computationally expensive) for model-based design, optimization, and control purposes and real-time (online) applications. Therefore, further model reductions are usually desired to achieve much more efficient models.

Two truncated models were studied: one based on the combined (averaged) constrained translational and rotational inertial completeness indices, shown in Fig. 8 for the first 50 modes, and one based on the combined (averaged) controllability indices, shown in Fig. 9 for the first 50 modes. In each case, the first 500 nonrigid (elastic) modes were looked at, evaluated, and ranked. Out of these, the first 15 elastic modes with the highest index values were kept to form the truncated model. These 15 elastic modes, summarized in Table 2, are in addition to the rigid modes corresponding to the six rigid body translations and rotations at the center of the solar sail (the origin of the body frame $\mathcal{F}_B$), which are kept as essential dynamic modes.

A dynamic example was considered to compare the performances of the truncated models against the full FEM-based linear structural model. It is assumed that the considered square solar sail, initially at rest, is exposed to a SRP of 4.56 μN/m^2 perpendicular to its surface that is formulated using the linear photonic thrust model [33]. There are also some (randomly generated) external point (concentrated) forces and moments applied to the sail at its center (origin of $\mathcal{F}_B$) and at its boom tips (where control vanes are attached). The point forces at the boom tips are intended to resemble the effect of control vanes [18,35]. This example is chosen such that different dynamic modes of the solar sail, expected to be excited by practical controllers in realistic maneuvers, are observable in the simulation results. To achieve this, the external point forces and moments (not the SRP) are about five to ten times larger than their real-world values.

To compare the models, the solar sail rigid body (central bus) translational and rotational velocities and displacements and the

booms 1 and 2 tip elastic translational velocities and displacements were calculated. The translational and rotational displacement plots did not show noticeable discrepancies between the responses of the two models. However, the velocity plots demonstrated significant differences between the response of the first truncated model and that of the full model. In particular, from the velocity comparison calculations, the second truncated model had a superior performance over the first truncated model in predicting the response of the considered 150 m square solar sail.

It is worth mentioning that each of the presented truncated models has only 21 DOF, 6 DOF corresponding to the rigid body modes and 15 DOF corresponding to the retained elastic modes. This is substantially less than DOF of the presented full structural model (about 6700 DOF). The truncated models are therefore significantly faster to solve (to integrate over time) than the full model and are ideal candidates for real-time simulation, model-based design parameter optimization, and (model-based) control development purposes. Both truncated models presented in this section are about 500 times faster than the full model.

IV. Noncollocated Attitude Controller

In this section, a simple noncollocated attitude controller will be developed for the 150 m square solar sail with control tip vanes, introduced and studied in the previous sections. The sensors are assumed to measure the attitude and rotational velocity of the solar sail at the central bus, and the actuators are assumed to be the control tip vanes with rotational DOF. For simplicity, the attitude controller is divided into three stages that are connected in series. At the first stage, a proportional-derivative (PD) controller will determine the required control torques from the solar sail desired orientation and current orientation and rotational velocity. At the second stage, a control allocation algorithm solves an underconstrained allocation problem to calculate the control forces that each of the four vanes has to provide from the required control torques. Finally, at the third stage, a nonlinear mapping and an optimization algorithm are used to derive the proper vane angles from the (scaled) vane control forces using the sun vector (i.e., the unit vector pointing from the sun to the solar sail). These stages are outlined in the block diagram of Fig. 10.

In Fig. 10, T_c is the vector of control torques, $f_{vs,c}$ is the column matrix of vanes control forces, $\alpha_{vs,c}$ is the column matrix of vanes control angles, $\{\varepsilon_d, \eta_d\}$ is the desired orientation quaternion, $\{\varepsilon, \eta\}$ is the current orientation quaternion, Ω is the vector of current rotational velocity in $\mathcal{F}_B$, and s is the current sun unit vector expressed in $\mathcal{F}_B$. As shown in Fig. 10, the attitude controller as a whole takes the desired orientation and current orientation and rotational velocity of the solar sail and returns the vane angles. For dynamic simulations, the vane angles devised by the attitude controller will be used to calculate the actual vane forces that, due to vane limitations and the actuators saturation, are usually different from (smaller than) the control vane forces calculated at the second stage. The attitude controller as a whole may be considered as a PD controller with actuator saturation. Below the saturation point, the controller would be asymptotically stable if the control torques were implemented using torquers on the central rigid hub.

In the following, the three stages of the proposed attitude controller will be explained in more detail, and an attitude maneuver will be
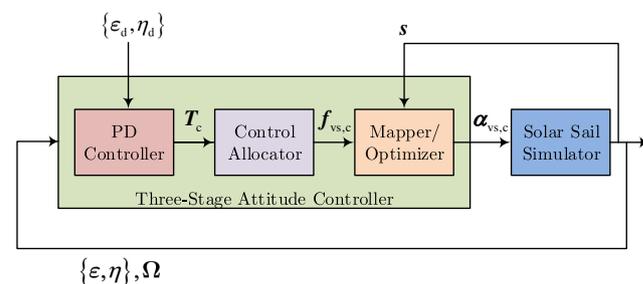
Fig. 10 Block diagram of three-stage attitude controller for the solar sail with control tip vanes.

considered to examine the controller and its interaction with the structural dynamics of the solar sail.

A. Stage 1: Proportional-Derivative Controller

A simple attitude controller suitable for both regulation (stabilization) and tracking control is the quaternion-based PD controller given as

$$
\begin{aligned}
\boldsymbol{T}_c = [T_{1,c} \quad T_{2,c} \quad T_{3,c}]^T &= -k\mathbb{1}(2\boldsymbol{\varepsilon}_e) - k'\mathbb{1}(\boldsymbol{\Omega}) \\
&= -2k\boldsymbol{\varepsilon}_e - k'\boldsymbol{\Omega}, \quad k, k' > 0
\end{aligned}
\tag{15}
$$

where $\boldsymbol{T}_c$ is the control torque vector described in $\mathcal{F}_B$, $\boldsymbol{\varepsilon}_e$ is the vector part of the attitude error quaternion, and k and k' are the proportional and derivative coefficients of the controller. The attitude error quaternion is calculated from the desired orientation quaternion $\{\boldsymbol{\varepsilon}_d, \eta_d\}$ and the current orientation quaternion $\{\boldsymbol{\varepsilon}, \eta\}$ as

$$
\begin{bmatrix} \boldsymbol{\varepsilon}_e \\ \eta_e \end{bmatrix} = \begin{bmatrix} \eta_d\mathbb{1} - \boldsymbol{\varepsilon}_d^{\times} & -\boldsymbol{\varepsilon}_d \\ \boldsymbol{\varepsilon}_d^T & \eta_d \end{bmatrix} \begin{bmatrix} \boldsymbol{\varepsilon} \\ \eta \end{bmatrix}
\tag{16}
$$

Note that for small (infinitesimal) rotations the vector part of a quaternion $\boldsymbol{\varepsilon}$ is half of the associated angle vector and the scalar part of it η is always 1 (can be dropped). For such cases, $2\boldsymbol{\varepsilon}_e$ in Eq. (15) would be equal to the vector of infinitesimal error angles, and for set point regulation at $\boldsymbol{\Theta}_d = \boldsymbol{0}$, one would have

$$
\boldsymbol{T}_c = -k\boldsymbol{\Theta}_e - k'\boldsymbol{\Omega} = -k\boldsymbol{\Theta} - k'\boldsymbol{\Omega}, \quad k, k' > 0
\tag{17}
$$

B. Stage 2: Control Allocator

Consider the 150 m square solar sail with control tip vanes studied in the previous sections. Assume that the sail attitude control is solely based on the tip-vane control forces and there is no point moment available at the central bus. Because of the small size of the vanes relative to the solar sail, the dynamics of the vanes can be neglected, and the control force generated on each vane can be simplified as a point control force vector $\boldsymbol{f}_{v,c}$ at the tip of the boom supporting that vane.

Now, as shown in Fig. 11, let a frame $\mathcal{F}_b$ to be attached to each boom at its tip (where a control vane is connected). The boom frame $\mathcal{F}_b$ is such that its first axis is parallel to the boom, pointing toward the outside of the solar sail, and its third axis is parallel to the third axis of the body frame $\mathcal{F}_B$. The second axis of each boom frame is so as to form a right-handed frame. Each boom frame rotates with the boom and solar sail but not with the vane. Using this boom frame $\mathcal{F}_b$, each vane's control force vector $\boldsymbol{f}_{v,c}$ may be represented as

$$
{}^b\boldsymbol{f}_{v,c} = [{}^bf_{1,v,c} \quad {}^bf_{2,v,c} \quad {}^bf_{3,v,c}]^T
\tag{18}
$$

Out of the three components of $\boldsymbol{f}_{v,c}$ in Eq. (18), only those perpendicular (lateral) to the support boom, i.e., ${}^bf_{2,v,c}$ and ${}^bf_{3,v,c}$, have noteworthy contribution to the dynamics of the solar sail and are

Fig. 11 Solar sail with four two-DOF control tip vanes along with body and vane frames.

of interest for attitude control purposes [18,35]. Therefore, a control allocation algorithm will be defined here to only determine these lateral control forces from the control torques. This allocation algorithm, devising the eight lateral control forces of the vanes from the three control torques, is simply formulated as

$$
{}^bf_{2,v1,c} = {}^bf_{2,v2,c} = {}^bf_{2,v3,c} = {}^bf_{2,v4,c} = \frac{T_{3,c}}{4L_b},
$$

$$
-{}^bf_{3,v1,c} = {}^bf_{3,v3,c} = \frac{T_{2,c}}{2L_b},
$$

$$
{}^bf_{3,v2,c} = -{}^bf_{3,v4,c} = \frac{T_{1,c}}{2L_b}
\tag{19}
$$

It is readily verified that the torques produced by these tip-vane forces about the mass center match $\boldsymbol{T}_c$ in the absence of sail and boom deformations.

C. Stage 3: Mapper/Optimizer

As mentioned earlier, each control vane of the considered 150 m square solar sail is assumed to be double-sided reflective and to have two angular DOF with respect to its support boom. Therefore, in total, there are eight independent control inputs to the solar sail. In general, if only attitude control is desired, one has to solve an underconstrained control allocation problem and a nonlinear mapping to find these eight control inputs, i.e., eight vane angles, from the three control torques [18,35]. However, in the three-stage attitude controller, a simple control allocation algorithm is first used to derive eight lateral vane forces from the three control torques. This control allocation algorithm is especially beneficial for the case in which each vane is assumed to have two angular DOF with respect to its support boom. With this allocation, it would be enough to only construct a mapping/optimization between the two lateral forces of each vane and its two angular DOF. The goal of the mapper/optimizer, as the third stage of the attitude controller, is to find the two vane angles such that the two actual lateral vane forces match the two control lateral vane forces, calculated by Eq. (19) in the second stage, as close as possible.

As shown in Fig. 11, the two angular DOF of each vane are denoted by α_1 and α_2, representing the rotations of the vane about the first and the second axes of the associated boom frame; each vane is first rotated about the second axis of $\mathcal{F}_b$ by α_2, followed by a rotation about the first axis of $\mathcal{F}_b$ by α_1. Since vanes are double-sided reflective, one can assume $-(\pi/2) \leq \alpha_1, \alpha_2 \leq (\pi/2)$. The assumed range for the vane angles can be justified by noting that rotation of a vane through larger angles does not lead to a new set of vane lateral forces that are not achievable by rotation angles within the assumed range and increases the chance of falling into situations in which the vane has almost no net effect (i.e., cases in which the vane is totally shadowed by the main sails or in which the vane shadow is completely on the main sails.

By assuming an ideal optical surface for the vanes that specularly reflects off the entirety of SRP, the force generated on each vane will be always normal to the vane surface. The vane (actual) force vector $\boldsymbol{f}_v$, potentially different from the vane control force vector $\boldsymbol{f}_{v,c}$ given by Eq. (18), can be expressed in $\mathcal{F}_b$ in terms of the vanes angles α_1 and α_2 as

$$
{}^b\boldsymbol{f}_v = \begin{bmatrix} {}^bf_{1,v} \\ {}^bf_{2,v} \\ {}^bf_{3,v} \end{bmatrix} = \|\boldsymbol{f}_v\|{}^b\boldsymbol{n}_v = \|\boldsymbol{f}_v\| \begin{bmatrix} \sin\alpha_2 \\ -\sin\alpha_1\cos\alpha_2 \\ \cos\alpha_1\cos\alpha_2 \end{bmatrix}
\tag{20}
$$

where $\|\square\|$ denotes the Euclidean norm (2-norm) operator and ${}^b\boldsymbol{n}_v$ is the normal unit vector of the vane surface described in $\mathcal{F}_b$. Note that $\|\boldsymbol{f}_v\|$ depends on the vane surface area, SRP magnitude, and orientation of the vane with respect to the sun, which itself is dependent on α_1, α_2, and $\boldsymbol{s}$ (i.e., the sun unit vector).

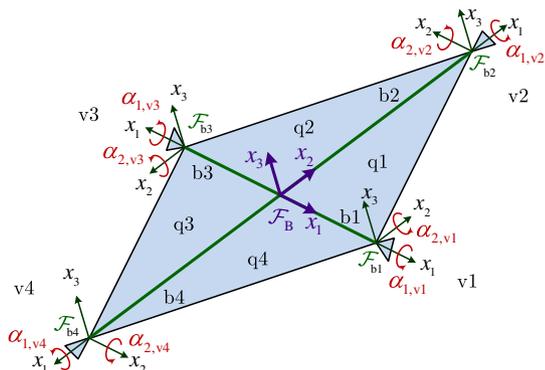Having the vane lateral control forces and recalling Eq. (20), one can use the relation

$$\alpha_1 = -\arctan\frac{{}^b f_{2,v,c}}{{}^b f_{3,v,c}}, \qquad -\frac{\pi}{2} \le \alpha_1 \le \frac{\pi}{2} \tag{21}$$

to first calculate α_1 and then use the single-variable optimization to find α_2,

$$\underset{\alpha_2}{\text{minimize}} \quad w_1({}^b f_{2,v,c} - {}^b f_{2,v})^2 + w_2({}^b f_{3,v,c} - {}^b f_{3,v})^2,$$
$$\text{subject to} \quad -\frac{\pi}{2} \le \alpha_2 \le \frac{\pi}{2} \tag{22}$$

where w_1 and w_2 are dimensionless weighting coefficients ($0 \le w_1$, $w_2 \le 1$) and note that ${}^b f_{2,v}$ and ${}^b f_{3,v}$ are relatively complex functions of α_1 and α_2 and s.

This simple approach, however, will face some difficulties when rotation of the vane by α_1, as calculated by Eq. (21), results in a situation in which, despite the value of α_2, the vane normal unit vector $\boldsymbol{n}_v$ is always perpendicular to the sun unit vector $\boldsymbol{s}$ and therefore $\|\boldsymbol{f}_v\| = 0$ for all values of α_2. For such cases, one may use the following (relatively more complex and harder-to-solve) two-variable optimization to find α_1 and α_2 at the same time:

$$\underset{\alpha_1,\alpha_2}{\text{minimize}} \quad w_1({}^b f_{2,v,c} - {}^b f_{2,v})^2 + w_2({}^b f_{3,v,c} - {}^b f_{3,v})^2,$$
$$\text{subject to} \quad -\frac{\pi}{2} \le \alpha_1 \le \frac{\pi}{2},$$
$$-\frac{\pi}{2} \le \alpha_2 \le \frac{\pi}{2} \tag{23}$$

It is worth mentioning that the two-variable optimization approach in Eq. (23) may permanently replace the single-variable optimization approach in Eqs. (21) and (22) for all cases. In either case, i.e., whether using Eqs. (21) and (22) with single-variable optimization or Eq. (23) with two-variable optimization, the problem is much easier to solve compared to the case without the control allocation algorithm (i.e., stage 2), which requires the solution of an eight-variable optimization problem. Additionally, one may use the approach taken by Choi and Damaren [35] to define an analytic convex form for the attainable force set of each vane and use that convex form within the single-variable and two-variable optimization problems. This will help with the convergence of numerical optimization algorithms used to solve the problems and can guarantee arrival to the global optimum point.

D. Dynamic Equations with Noncollocated Attitude Controller

Consider the square solar sail with control tip vanes and the explained noncollocated attitude controller. The eight lateral forces of four tip vanes may be combined as a control input vector $\boldsymbol{z}$,

$$\boldsymbol{z} = [{}^b f_{2,v1} \quad {}^b f_{3,v1} \quad {}^b f_{2,v2} \quad {}^b f_{3,v2} \quad {}^b f_{2,v3} \quad {}^b f_{3,v3} \quad {}^b f_{2,v4} \quad {}^b f_{3,v4}]^T \tag{24}$$

and used to rewrite the dynamic equations in Eq. (10) as

$$\mathcal{M}\ddot{q} + \mathcal{K}q = \mathcal{Q} + \mathcal{B}z \tag{25}$$

where the control input matrix $\mathcal{B}$ would have eight columns corresponding to the eight lateral vane forces in $\boldsymbol{z}$ and the generalized force matrix $\mathcal{Q}$ will contain the effect of noncontrol external forces and moments, such as the solar radiation pressure and the first components of the vanes forces in $\mathcal{F}_b$ (i.e., ${}^b f_{1,v1}$, ${}^b f_{1,v2}$, ${}^b f_{1,v3}$, and ${}^b f_{1,v4}$).

As mentioned earlier, the sensors are assumed to measure the attitude and rotational velocity of the solar sail at the central bus, and assuming small rigid body rotations, the measurement vectors are

$$\boldsymbol{y} = \mathcal{C}q = \boldsymbol{\Theta}, \qquad \boldsymbol{y}' = \mathcal{C}'\dot{q} = \boldsymbol{\Omega} \tag{26}$$

and the control torque is

$$\boldsymbol{T}_c = -k\boldsymbol{\Theta} - k'\boldsymbol{\Omega} = -k\boldsymbol{y} - k'\boldsymbol{y}', \qquad k, k' > 0 \tag{27}$$

Below the saturation point, for each vane, the actual lateral forces ${}^b f_{2,v}$ and ${}^b f_{3,v}$ and the control lateral forces ${}^b f_{2,v,c}$ and ${}^b f_{3,v,c}$ become equal, and recalling Eq. (19), one can write

$$\boldsymbol{z} = \frac{1}{4L_b}\begin{bmatrix} 0 & 0 & 0 & 0 & 2 & 0 & 0 & 0 \\ 0 & -2 & 0 & 0 & 0 & 2 & 0 & 0 \\ 1 & 0 & 1 & 0 & 1 & 0 & 1 & 0 \end{bmatrix}^T \begin{bmatrix} T_{1,c} \\ T_{2,c} \\ T_{3,c} \end{bmatrix} = \boldsymbol{F}\boldsymbol{T}_c \tag{28}$$

where $\boldsymbol{F}$ is the torque-to-force-conversion matrix and L_b is the boom length.

By combining Eqs. (25–28), the integrated dynamic equations of the solar sail and the noncollocated controller will be obtained as

$$\mathcal{M}\ddot{q} + \mathcal{B}Fk'\mathcal{C}'\dot{q} + (\mathcal{K} + \mathcal{B}Fk\mathcal{C})q = \mathcal{Q} \tag{29}$$

In Eq. (29), there is no guarantee that the matrices $\mathcal{B}Fk\mathcal{C}$ and $\mathcal{B}Fk'\mathcal{C}'$ are symmetric and positive semidefinite. In fact, one can show that both matrices would have symmetric parts with some positive and some (small) negative eigenvalues. The negative eigenvalues correspond to negative stiffness and damping effects added to some of the elastic modes of the solar sail and may destabilize the solar sail. The negative damping effects are more critical considering the fact that the solar sail has a very limited structural damping and its elastic modes, if at all, are only slightly damped. One can conclude that the noncollocated attitude controller may destabilize the solar sail through interaction with the structural dynamics of the spacecraft (this is also known as the control and observation spillover [32,36]).
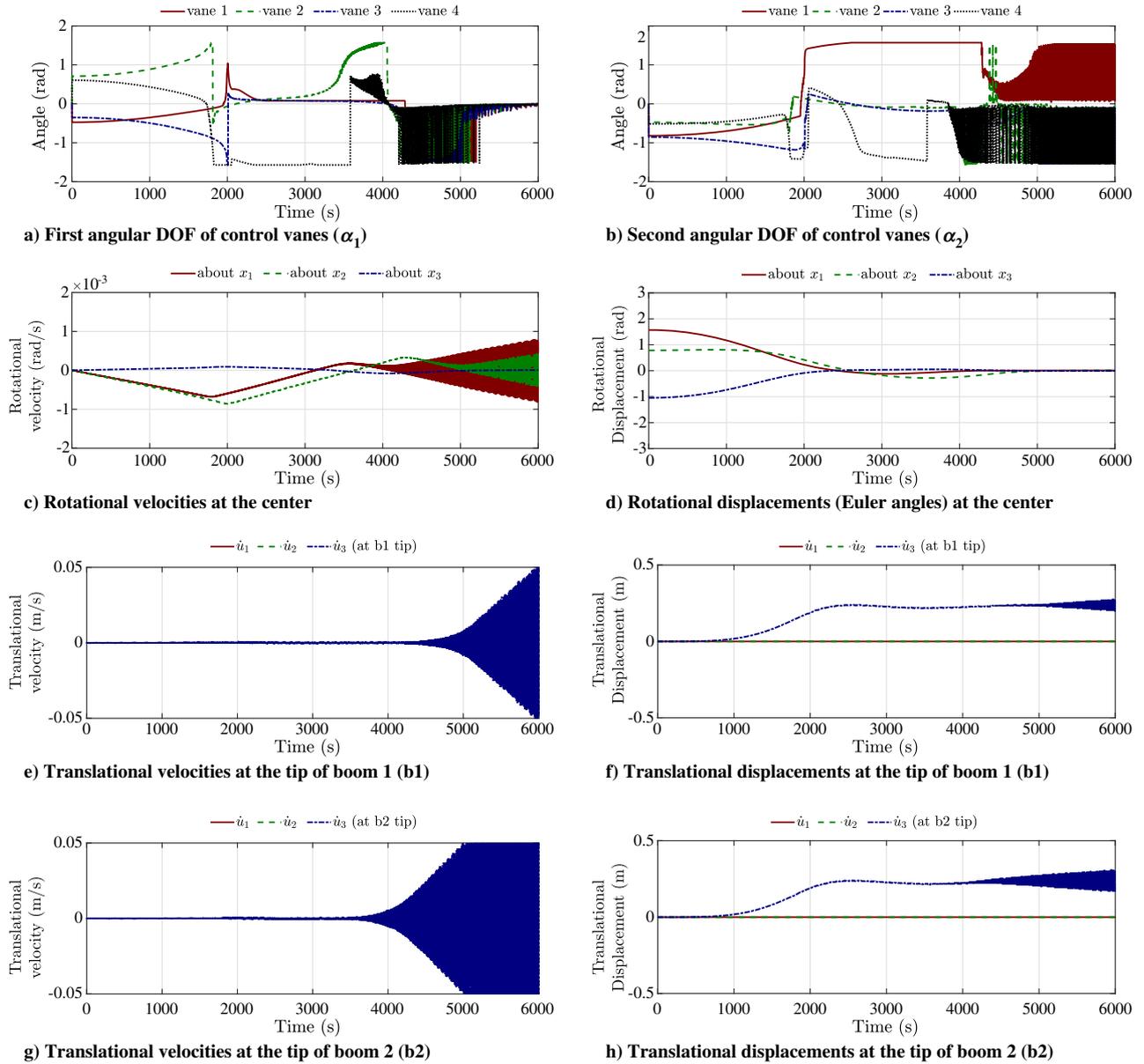
E. Attitude Control Maneuver

To illustrate the performance of the developed noncollocated attitude controller, an attitude maneuver will be presented in this section. In the maneuver, the solar sail, initially at rest, starts from an orientation with x_1–x_2–x_3 Euler angles of $\theta_1 = \pi/2$, $\theta_2 = \pi/4$, and $\theta_3 = -(\pi/3)$, and it is desired to rotate the sail to a final orientation in which $\theta_1 = \theta_2 = \theta_3 = 0$. The desired orientation is given to the controller as a step input (without any input shaping). During the maneuver, the solar sail is under the action of a SRP of $4.56~\mu\text{N/m}^2$ (formulated using the linear photonic thrust model [33]) that is perpendicular to the sail surface when $\theta_1 = \theta_2 = \theta_3 = 0$. The controller coefficients are chosen to be $k = 5~\text{N} \cdot \text{m}$ and $k' = 2500~(\text{N} \cdot \text{m} \cdot \text{s})/\text{rad}$, and the optimization weighting coefficients are set to be $w_1 = w_2 = 1/2$. The two-variable optimization approach, given by Eq. (23), is employed in the maneuver. The optimization problem is solved using a particle swarm optimization algorithm toolbox [37]. It is worth noting that attitude control strategies relying on SRP and a controlled offset between the solar sail's center of mass and center of pressure (e.g., strategies that use sliding and gimballed masses) provide no attitude control at the considered initial condition, when the sun is near the edge of the solar sail, and cannot handle this maneuver.

The control vane angles and the dynamic response of the solar sail during the attitude maneuver are plotted in Fig. 12. The results are obtained by employing the full FEM-based linear structural model of the solar sail. Although the controller proves to be capable of rotating the solar sail to the desired orientation, one may notice that the controller interaction with the structural dynamics of the spacecraft results in some instability after a while. This is more obvious in the velocity plots of Fig. 12 after about $t = 4000$ s.

V. Collocated Attitude Controller

A more advanced attitude controller without worrying about control and observation spillover may be designed for the considered 150 m square solar sail by assuming the measurement sensors to be collocated with the control actuators, i.e., tip vanes. Recall that, with the eight lateral forces of four tip vanes forming the control vector $\boldsymbol{z}$, the dynamic equations of the solar sail are given by Eq. (25). Now,

a) **First angular DOF of control vanes (α_1)**

b) **Second angular DOF of control vanes (α_2)**

c) **Rotational velocities at the center**

d) **Rotational displacements (Euler angles) at the center**

e) **Translational velocities at the tip of boom 1 (b1)**

f) **Translational displacements at the tip of boom 1 (b1)**

g) **Translational velocities at the tip of boom 2 (b2)**

h) **Translational displacements at the tip of boom 2 (b2)**

Fig. 12   Solar sail dynamics with a noncollocated attitude controller (represented in $\mathcal{F}_B$) during the attitude maneuver from $\theta_1 = \pi/2$, $\theta_2 = \pi/4$, $\theta_3 = -(\pi/3)$ to $\theta_1 = \theta_2 = \theta_3 = 0$.

to form a collocated (passive) system, the sensor measurements should take the form

$$y = \mathcal{C}q = \mathcal{B}^T q, \qquad y' = \mathcal{C}'\dot{q} = \mathcal{B}^T \dot{q} \qquad (30)$$

One can show that, assuming small rigid body rotations, the measurement vectors y and y' would correspond to the total translational displacements and velocities in the directions of the vanes lateral forces, i.e.,

$$y = [{}^b p_{2,v1} \quad {}^b p_{3,v1} \quad {}^b p_{2,v2} \quad {}^b p_{3,v2} \quad {}^b p_{2,v3} \quad {}^b p_{3,v3} \quad {}^b p_{2,v4} \quad {}^b p_{3,v4}]^T,$$
$$y' = [{}^b \dot{p}_{2,v1} \quad {}^b \dot{p}_{3,v1} \quad {}^b \dot{p}_{2,v2} \quad {}^b \dot{p}_{3,v2} \quad {}^b \dot{p}_{2,v3} \quad {}^b \dot{p}_{3,v3} \quad {}^b \dot{p}_{2,v4} \quad {}^b \dot{p}_{3,v4}]^T$$
$$(31)$$

where Eqs. (4) and (5) are recalled. Using the measurements y and y', the solar sail overall (average) attitude and rotational velocity can be obtained as

$$\bar{\Theta}_1 = \frac{1}{2L_b}({}^b p_{3,v2} - {}^b p_{3,v4}),$$

$$\bar{\Theta}_2 = \frac{1}{2L_b}({}^b p_{3,v3} - {}^b p_{3,v1}),$$

$$\bar{\Theta}_3 = \frac{1}{4L_b}({}^b p_{2,v1} + {}^b p_{2,v2} + {}^b p_{2,v3} + {}^b p_{2,v4}),$$

$$\bar{\Omega}_1 = \frac{1}{2L_b}({}^b \dot{p}_{3,v2} - {}^b \dot{p}_{3,v4}),$$

$$\bar{\Omega}_2 = \frac{1}{2L_b}({}^b \dot{p}_{3,v3} - {}^b \dot{p}_{3,v1}),$$

$$\bar{\Omega}_3 = \frac{1}{4L_b}({}^b \dot{p}_{2,v1} + {}^b \dot{p}_{2,v2} + {}^b \dot{p}_{2,v3} + {}^b \dot{p}_{2,v4}) \qquad (32)$$

or in the matrix form

$$\bar{\Theta} = Ry = F^T y,$$
$$\bar{\Omega} = Ry' = F^T y' \qquad (33)$$

where $R = F^T$ is the translational to rotational coordinates conversion matrix and recall that F is the torque-to-force-conversion matrix defined in Eq. (28). Now, a PD control law can be defined to calculate the required control torque as

$$T_c = -k\bar{\Theta} - k'\bar{\Omega} = -kF^T y - k'F^T y' \quad (34)$$

This can replace the PD control law (stage 1) of the noncollocated attitude controller in the previous section and can combine with the control allocator and mapper/optimizer defined there (stages 2 and 3) to form a complete collocated attitude controller that calculates the control vanes angles from the measurement vectors.

Again, below the saturation point, the control input vector (containing the vanes lateral control forces) would be

$$z = FT_c \quad (35)$$

and by combining Eqs. (33–35) with Eq. (25), the integrated dynamic equations of the solar sail and the collocated attitude controller will become

$$\mathcal{M}\ddot{q} + \mathcal{B}Fk'F^T\mathcal{B}^T\dot{q} + (\mathcal{K} + \mathcal{B}FkF^T\mathcal{B}^T)q = \mathcal{Q} \quad (36)$$

where note that for $k, k' > 0$ matrices $\mathcal{B}FkF^T\mathcal{B}^T$ and $\mathcal{B}Fk'F^T\mathcal{B}^T$ are symmetric and positive semidefinite. One can conclude that the collocated controller is only adding positive stiffness and damping effects to rigid body rotations and some of the elastic modes of the solar sail and may not destabilize the spacecraft. Such a controller would not result in any spillover issues.

Analogous to the noncollocated controller case, for large rigid body rotations and attitude tracking control purposes, the infinitesimal rotation vector Θ should be replaced with twice the vector part of the attitude error quaternion, i.e., $2\varepsilon_e$, calculated using the desired orientation quaternion $\{\varepsilon_d, \eta_d\}$ and the current orientation quaternion $\{\varepsilon, \eta\}$. In fact, one can show that $F^T y$ contains contributions from the rigid body rotations at the solar sail center and from some of the elastic modes, and in practice, the contribution of rigid body rotations should be replaced with $2\varepsilon_e$.
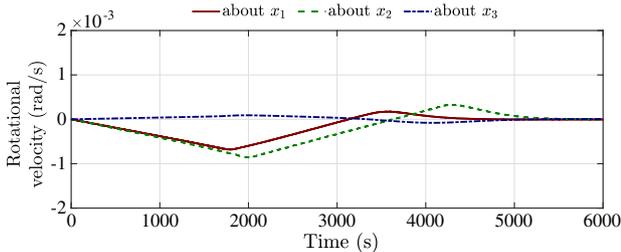
Consider again the attitude control maneuver explained in the previous section. Employing the developed collocated attitude controller, the control vane angles and the dynamic response of the solar sail during this maneuver are plotted in Fig. 13. One may observe that, with the collocated controller, no spillover instability occurs during the attitude maneuver.
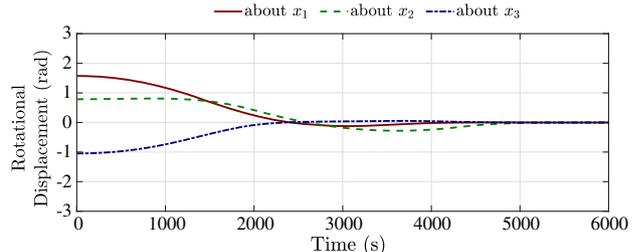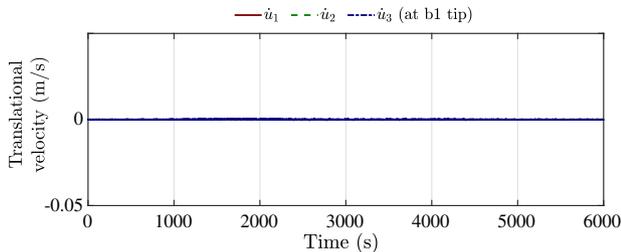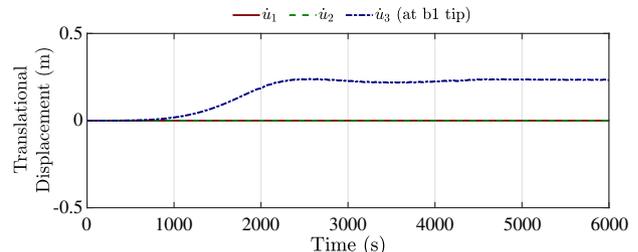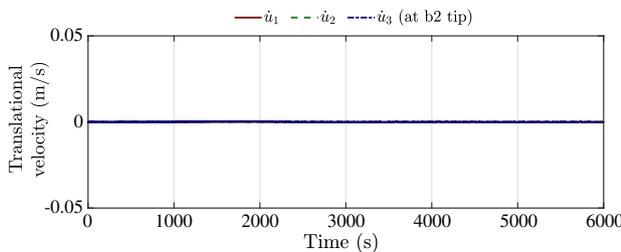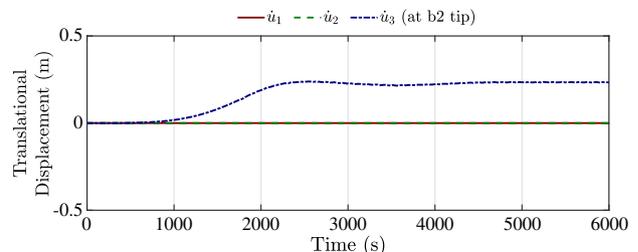

Fig. 13 Solar sail dynamics with a collocated attitude controller (represented in $\mathcal{F}_B$) during the attitude control maneuver from $\theta_1 = \pi/2, \theta_2 = \pi/4, \theta_3 = -(\pi/3)$ to $\theta_1 = \theta_2 = \theta_3 = 0$.

VI. Conclusions

A new approach has been taken to develop a two-stage linear model for structural dynamics of a square solar sail with pretensioned sails supported by flexible diagonal booms. In the model, a static finite element or analytic model was first employed to calculate the static in-plane stresses in the pretensioned sails. Then, a dynamic finite element model calculated the in- and out-of-plane deformations and displacements of the solar sail by taking into account the effect of static in-plane stresses calculated by the static finite element or analytic model. This linear model is valuable since it allows for powerful tools and theories to be used for modal analysis, model truncation (order reduction), and model-based controller development.

The linear model was used to study a 150 m square solar sail with two-degrees of freedom (DOF) control tip vanes. The constrained and unconstrained mode shapes of the selected sail were presented, and modal cost analyses based on different criteria were used to evaluate and rank these modes. The constrained inertial completeness index proved to be an effective criterion to evaluate the elastic modes. The mode shapes were also examined based on controllability and observability indices, and it was disclosed that with control tip vanes and boom tips velocity measurements most of the elastic modes of the solar sail are controllable and observable.

Results of the modal cost analysis based on constrained inertial completeness index and controllability index were used to derive two truncated (reduced-order) structural dynamic models for the solar sail. Dynamic simulations showed that both reduced models, with only 21 DOF, were reasonably accurate when predicting the translational and rotational displacements of the solar sail. It is noteworthy that accurate prediction of these rigid body motions is of great importance for trajectory (orbital) and attitude control of solar sails. For predicting the translational and rotational velocities, however, the truncated model based on the controllability index proved to be much more accurate. These truncated models can be used for model-based attitude and shape (vibration suppression) controller developments.

Two attitude controllers, with noncollocated and collocated actuators and sensors, were also presented for the (undamped) 150 m square solar sail with two-DOF control tip vanes. Both controllers had a three-stage structure including a proportional-derivative controller to calculate needed control torque from the current attitude and rotational velocity, a control allocator to determine eight lateral control forces of four vanes from the needed control torque, and a (nonlinear) mapper/optimizer to find the two angles of each vane from its two lateral control forces. Both controllers proved to be capable of reorienting the solar sail to the desired attitude. However, the noncollocated controller showed signs of destabilizing the dynamics of the undamped solar sail due to control and observation spillovers. This was not the case with the collocated controller, which is known to be spillover proof. Finally, it should be noted that none of the presented controllers was designed to exclusively damp the elastic modes of the solar sail. Developing such controllers is left to a future work.

Acknowledgments

References

[1] Fu, B., Sperber, E., and Eke, F., "Solar Sail Technology: A State of the Art Review," *Progress in Aerospace Sciences*, Vol. 86, Oct. 2016, pp. 1–19.
doi:10.1016/j.paerosci.2016.07.001

[2] McInnes, C., *Solar Sailing: Technology, Dynamics, and Mission Applications*, Springer–Verlag, New York, 1999.
doi:10.1007/978-1-4471-3992-8

[3] Garwin, R., "Solar Sailing: A Practical Method of Propulsion Within the Solar System," *Jet Propulsion*, Vol. 28, No. 3, 1958, pp. 188–196.
doi:10.2514/8.7271

[4] Wie, B., "Solar Sail Attitude Control and Dynamics, Part 1," *Journal of Guidance, Control, and Dynamics*, Vol. 27, No. 4, 2004, pp. 526–535.
doi:10.2514/1.11134

[5] Wie, B., "Solar Sail Attitude Control and Dynamics, Part 2," *Journal of Guidance, Control, and Dynamics*, Vol. 27, No. 4, 2004, pp. 536–544.
doi:10.2514/1.11133

[6] Sleight, D., and Muheim, D., "Parametric Studies of Square Solar Sails Using Finite Element Analysis," *45th AIAA/ASME/ASCE/AHS/ASC Structures, Structural Dynamics & Materials Conference*, AIAA Paper 2004-1509, April 2004.
doi:10.2514/6.2004-1509

[7] McInnes, C., "Solar Sailing: Mission Applications and Engineering Challenges," *Philosophical Transactions of the Royal Society of London A: Mathematical, Physical and Engineering Sciences*, Vol. 361, No. 1813, 2003, pp. 2989–3008.
doi:10.1098/rsta.2003.1280

[8] Macdonald, M., *Solar Sailing: Applications and Technology Advancement, Advances in Spacecraft Technologies*, InTech, Rijeka, Croatia, 2011, pp. 35–60, http://strathprints.strath.ac.uk/id/eprint/31455.

[9] Smith, S., Song, H., Baker, J., Black, J., and Muheim, D., "Flexible Models for Solar Sail Control," *46th AIAA/ASME/ASCE/AHS/ASC Structures, Structural Dynamics & Materials Conference*, AIAA Paper 2005-1801, April 2005.
doi:10.2514/6.2005-1801

[10] Liu, J., Cui, N., Shen, F., and Rong, S., "Dynamics of Highly-Flexible Solar Sail Subjected to Various Forces," *Acta Astronautica*, Vol. 103, Oct.–Nov. 2014, pp. 55–72.
doi:10.1016/j.actaastro.2014.06.030

[11] Eldad, O., Lightsey, E., and Claudel, C., "Minimum-Time Attitude Control of Deformable Solar Sails with Model Uncertainty," *Journal of Spacecraft and Rockets*, Vol. 54, No. 4, 2017, pp. 863–870.
doi:10.2514/1.A33713

[12] Taleghani, B., Sleight, D., Muheim, D., Belvin, K., and Wang, J., "Assessment of Analysis Approaches for Solar Sail Structural Response," *39th AIAA/ASME/SAE/ASEE Joint Propulsion Conference and Exhibit*, AIAA Paper 2003-4796, July 2003.
doi:10.2514/6.2003-4796

[13] Sleight, D., Michii, Y., Lichodziejewski, D., Derbes, B., Mann, T., Slade, K., and Wang, J., "Structural Analysis of an Inflation-Deployed Solar Sail with Experimental Validation," *41st AIAA/ASME/SAE/ASEE Joint Propulsion Conference & Exhibit*, AIAA Paper 2005-3727, July 2005.
doi:10.2514/6.2005-3727

[14] Miyazaki, Y., and Iwai, Y., "Dynamics Model of Solar Sail Membrane," *ISAS 14th Workshop on Astrodynamics and Flight Mechanics*, Sagamihara, Japan, July 2004, pp. 32–37, http://www.muses-c.isas.ac.jp/kawalab/astro/pdf/2004A_6.pdf.

[15] Miyazaki, Y., "Wrinkle/Slack Model and Finite Element Dynamics of Membrane," *International Journal for Numerical Methods in Engineering*, Vol. 66, No. 7, 2006, pp. 1179–1209.
doi:10.1002/(ISSN)1097-0207

[16] Sakamoto, H., Miyazaki, Y., and Park, K., "Finite Element Modeling of Sail Deformation Under Solar Radiation Pressure," *Journal of Spacecraft and Rockets*, Vol. 44, No. 3, 2007, pp. 514–521.
doi:10.2514/1.23474

[17] Choi, M., and Damaren, C., "Structural and Attitude Dynamics and Control of a Solar Sail Using Two Degrees of Freedom Tip Vanes," *AIAA SciTech Forum, 2nd AIAA Spacecraft Structures Conference*, AIAA Paper 2015-0433, Jan. 2015.
doi:10.2514/6.2015-0433

[18] Choi, M., and Damaren, C., "Structural Dynamics and Attitude Control of a Solar Sail Using Tip Vanes," *Journal of Spacecraft and Rockets*, Vol. 52, No. 6, 2015, pp. 1665–1679.
doi:10.2514/1.A33179

[19] Li, Q., Ma, X., and Wang, T., "Reduced Model for Flexible Solar Sail Dynamics," *Journal of Spacecraft and Rockets*, Vol. 48, No. 3, 2011, pp. 446–453.
doi:10.2514/1.48789

[20] Zhang, J., Zhai, K., and Wang, T. S., "Control of Large Angle Maneuvers for the Flexible Solar Sail," *Science China Physics, Mechanics and Astronomy*, Vol. 54, No. 4, 2011, pp. 770–776.
doi:10.1007/s11433-011-4277-1

[21] Liu, J., Cui, N., Shen, F., Rong, S., and Wen, X., "Dynamic Modeling and Analysis of a Flexible Sailcraft," *Advances in Space Research*, Vol. 56, No. 4, 2015, pp. 693–713.
doi:10.1016/j.asr.2015.05.011

[22] Skelton, R., and Hughes, P., "Modal Cost Analysis for Linear Matrix-Second-Order Systems," *Journal of Dynamic Systems, Measurement, and Control*, Vol. 102, No. 3, 1980, pp. 151–158.
doi:10.1115/1.3139625

[23] Hughes, P., and Skelton, R., "Modal Truncation for Flexible Spacecraft," *Journal of Guidance, Control, and Dynamics*, Vol. 4, No. 3, 1981, pp. 291–297.
doi:10.2514/3.56081

[24] Skelton, R., Hughes, P., and Hablani, H., "Order Reduction for Models of Space Structures Using Modal Cost Analysis," *Journal of Guidance, Control, and Dynamics*, Vol. 5, No. 4, 1982, pp. 351–357.
doi:10.2514/3.19773

[25] Greschik, G., and Mikulas, M., "Design Study of a Square Solar Sail Architecture," *Journal of Spacecraft and Rockets*, Vol. 39, No. 5, 2002, pp. 653–661.
doi:10.2514/2.3886

[26] Johnson, L., Young, R., Montgomery, E., and Alhorn, D., "Status of Solar Sail Technology Within NASA," *Advances in Space Research*, Vol. 48, No. 11, 2011, pp. 1687–1694.
doi:10.1016/j.asr.2010.12.011

[27] Hassanpour, S., and Damaren, C., "Linear Structural Dynamics and Modal Cost Analysis for a Solar Sail," *AIAA SciTech Forum, 5th AIAA Spacecraft Structures Conference*, AIAA Paper 2018-1434, 2018.

[28] Timoshenko, S., and Woinowsky-Krieger, S., *Theory of Plates and Shells*, 2nd ed., McGraw–Hill, New York, 1959, pp. 378–428.

[29] Shames, I., and Dym, C., *Energy and Finite Element Methods in Structural Mechanics*, Taylor & Francis, New York, 1985, pp. 487–614.

[30] Zienkiewicz, O., *The Finite Element Method in Engineering Science*, 2nd ed., McGraw–Hill, New York, 1971, pp. 16–211.

[31] Hassanpour, S., and Heppler, G., "Approximation of Infinitesimal Rotations in Calculus of Variations," *Journal of Guidance, Control, and Dynamics*, Vol. 39, No. 1, 2016, pp. 703–710.
doi:10.2514/1.G001041

[32] Balas, M., "Trends in Large Space Structure Control Theory: Fondest Hopes, Wildest Dreams," *IEEE Transactions on Automatic Control*, Vol. 27, No. 3, 1982, pp. 522–535.
doi:10.1109/TAC.1982.1102953

[33] Greschik, G., "A Linear Photonic Thrust Model and Its Application to the L'Garde Solar Sail Surface," *54th AIAA/ASME/ASCE/AHS/ASC Structures, Structural Dynamics & Materials Conference*, AIAA Paper 2013-1803, April 2013.
doi:10.2514/6.2013-1803

[34] Choi, M., and Damaren, C., "Control Allocation of Solar Sail Tip Vanes with Two Degrees of Freedom Using Elliptical Constraints," *AIAA Guidance, Navigation, and Control Conference*, AIAA Paper 2012-5002, Aug. 2012.
doi:10.2514/6.2012-5002

[35] Choi, M., and Damaren, C., "Control Allocation of Solar Sail Tip Vanes with Two Degrees of Freedom," *Journal of Guidance, Control, and Dynamics*, Vol. 39, No. 8, 2016, pp. 1857–1865.
doi:10.2514/1.G001703

[36] Balas, M., "Feedback Control of Flexible Systems," *IEEE Transactions on Automatic Control*, Vol. 23, No. 4, 1978, pp. 673–679.
doi:10.1109/TAC.1978.1101798

[37] Birge, B., "PSOt: A Particle Swarm Optimization Toolbox for Use with Matlab," *Proceedings of the 2003 IEEE Swarm Intelligence Symposium*, Indianapolis, IN, April 2003, pp. 182–186.
doi:10.1109/SIS.2003.1202265